Nano Energy 49 (2018) 247–256

Contents lists available at ScienceDirect

Nano Energy

journal homepage: www.elsevier.com/locate/nanoen

Full paper

Enhanced piezoelectric output performance via control of dielectrics in Fe^{2+}-incorporated $MAPbI_3$ perovskite thin films: Flexible piezoelectric generators

Swathi Ippili[a,1], Venkatraju Jella[a,1], Jaegyu Kim[b], Seungbum Hong[b], Soon-Gil Yoon[a,*]

[a] Department of Materials Science and Engineering, Chungnam National University, Daeduk Science Town, 34134 Daejeon, Republic of Korea
[b] Materials Imaging and Integration Lab., Department of materials Science and Engineering, Korea Advanced Institute of Science and Technology (KAIST), 291, Daehak-ro, Yuseong-gu, Daejeon 34141, Republic of Korea

ARTICLE INFO

Keywords:
Fe^{2+}-incorporated $MAPbI_3$ perovskite
Phase transition
Dielectric property
Piezoelectric generator

ABSTRACT

We report a high-performance flexible piezoelectric generator (PEG) that was based on organic-inorganic lead halide perovskite materials and is operated by controlling the dielectric constant via the partial substitution of Pb^{2+} with Fe^{2+} in $MAPbI_3$. The partial replacement of Pb^{2+} with Fe^{2+} improved both the morphology and crystallinity of $MAPb_{1-x}Fe_xI_3$ ($0.01 \le x \le 0.50$) films that undergo a tetragonal-cubic phase transition above an incorporated concentration of Fe^{2+} ($x > 0.07$). In addition, the phase transition temperatures of $MAPb_{1-x}Fe_xI_3$ ($0.01 \le x \le 0.07$) films linearly decreased as a function of incorporated concentration, which resulted in a transition temperature for $MAPb_{1-x}Fe_xI_3$ ($x = 0.07$) of ~ 45.5 ± 1.5 °C. The dielectric properties as a function of incorporated concentration at room temperature suggested that $MAPb_{1-x}Fe_xI_3$ ($x = 0.07$) exhibited a dielectric constant of ~107 and a dissipation factor of 0.02 at 100 kHz. The $MAPb_{1-x}Fe_xI_3$ ($x = 0.07$) films exhibited a low leakage current density of ~ 10^{-6} at a high applied electric field of 40 kV/cm, and the resultant remanent polarization from saturated ferroelectric P-E hysteresis loops was ~ 1.6 μC/cm^2. The $MAPb_{1-x}Fe_xI_3$ ($x = 0.07$) flexible PEG improved output performance by ~ 7.29 V and current density by ~ 0.88 μA/cm^2 after poling at 30 kV/cm. This was sufficient to instantly light a commercial light-emitting diode (LED) without a storage device. This approach provides a framework that enhances the output performance of organic-inorganic metal halide perovskite materials-based piezoelectric energy harvesters, which could help pave the road to viable, self-powered, wearable electronics.

1. Introduction

In recent years, many researchers have explored the viability of various energy harvesters to power small-scale, wearable and portable electronic devices. In particular, solar [1], thermoelectric [2], triboelectric [3], and piezoelectric [4] devices have been widely investigated as sustainable energy harvesting approaches to scavenge energy from the ambient environment and biomechanical movement. For many years, PEGs have ranked among the most promising of power sources for mechanical energy conversion. The types of nanostructured piezoelectric materials that have been used in the fabrication of PEGs include semiconductors (ZnO [5], GaN [6], ZnS [7], CdS [8], etc.), ceramics (PZT [9], PMN-PT [10], $NaNbO_3$ [11], $ZnSnO_3$ [12], etc.), and polymers (PVDF [13] and copolymers [14]). Among these, piezoelectric materials with perovskite structures and high piezoelectric constants such as PZT, $BaTiO_3$, etc., have proven to be excellent candidates for piezoelectric application [15,16]. These conventional inorganic piezoelectric materials, however, require complicated synthesis processes such as high-temperature calcination and sintering.

Organic-inorganic lead halide perovskite materials (ABX_3, A = organic monovalent cation (MA = CH_3NH_3, or FA = CH $(NH_2)_2$), B = divalent metal cation (Pb) and X = halide anion (Cl, Br, I,)) are now being extensively examined for applications to photovoltaics [17], photodetectors [18], light emitting diodes [19], thin film transistors [20], and lasers [21]. These materials offer unique properties as well as inexpensive, low-temperature solution-based processing [22]. The certified power conversion efficiency of $MAPbI_3$-based perovskite solar cells has recently been raised to more than 22.1% [23]. Recently, organic-inorganic lead halide perovskite materials have been studied for piezoelectric applications because of their prominent ferroelectric and

* Corresponding author.
E-mail address: sgyoon@cnu.ac.kr (S.-G. Yoon).
[1] Both authors contributed equally to this work.

https://doi.org/10.1016/j.nanoen.2018.04.031
Received 14 February 2018; Received in revised form 4 April 2018; Accepted 9 April 2018
Available online 22 April 2018
2211-2855/ © 2018 Elsevier Ltd. All rights reserved.

piezoelectric responses [24]. Piezoelectric properties of organic-inorganic perovskite materials were theoretically investigated with chemical substitution [25]. Coll *et al.* observed polarization switching and light-enhanced piezoelectricity in $MAPbI_3$ films [26]. Kim et al. reported the first viable PEG using $MAPbI_3$ thin films with output voltage and current density values of 2.7 V and 140 nA cm^{-2}, respectively, whereas the dielectric permittivity of these $MAPbI_3$ polycrystalline films was about 52 at 1 MHz [27]. However, there is a lack of studies concerning the dopant or incorporation effect on the dielectric and piezoelectric properties of organic-inorganic metal halide perovskite materials. Moreover, toxicity and stability issues with organic-inorganic lead halide-based devices have been barriers to their commercialization. Therefore, it is necessary to develop either partial-lead or lead-free perovskite materials for the fabrication of efficient, stable and environmentally friendly energy-harvesting devices for everyday practical applications.

In this work, we developed a high-performance thin film PEG that partially replaces lead (Pb^{2+}) with iron (Fe^{2+}) in $MAPbI_3$. We studied the crystal structure, morphology, absorbance, and photoluminescence properties of various Fe^{2+}-incorporated $MAPbI_3$ perovskite thin films in detail. The structural phase changes were investigated via temperature-dependent X-ray diffraction (XRD) and correlated with the Curie temperature of various Fe^{2+}-incorporated $MAPbI_3$ films. The dielectric constant of Fe^{2+}-incorporated $MAPbI_3$ films was significantly changed with incorporated concentration. Fe^{2+}-incorporated $MAPbI_3$ film-based PEGs were fabricated using flexible Au/Ti/polyimide (PI) and ITO/polyethylene terephthalate (PET) substrates as top- and bottom-electrodes, and the piezoelectric output performance was investigated as a function of Fe^{2+}-incorporated concentration.

2. Experimental section

2.1. Materials used in the synthesis of $MAPb_{1-x}Fe_xI_3$ ($0 \le x \le 0.50$) precursors

All the purchased materials were used without further purification for synthesis of the following perovskite precursors: Lead(II) acetate trihydrate ($Pb(OAc)_2{\cdot}3H_2O$, 99.999% Alfa Aesar), Iron(II) acetate ($Fe(OAc)_2$), Hydroiodic acid (HI, 57% in water, Alfa Aesar), Methyl amine (40% in aqueous solution, Sigma Aldrich), N,N-dimethylformamide (DMF, anhydrous, 99.8%, Sigma Aldrich), Toluene (99.7%, Dae-Jung chemicals and metals co., LTD), and Diethyl ether (ACS reagent, anhydrous ≥99%, Sigma Aldrich).

2.2. Methyl ammonium iodide (MAI) synthesis

20 mL of hydroiodic acid was added drop-wise to a 20 mL solution of Methyl amine at 0 °C. The solution was maintained with constant stirring for 2 h. The precipitate was then recovered by evaporating the solvent. This light-yellow solid was rinsed with a minimum amount of ethanol and precipitated using diethyl ether. This process was repeated 3 times to remove unreacted raw additives. The resultant white precipitate was collected and dried in a vacuum oven at 60 °C for 24 h.

2.3. Synthesis of $MAPb_{1-x}Fe_xI_3$ precursors

Mixed-metal perovskite precursor solutions of $MAPb_{1-x}Fe_xI_3$ with x = 0–0.50 were freshly prepared by mixing MAI, Lead(II) acetate trihydrate, and Iron(II) acetate in N,N-dimethylformamide (DMF) solvent in a 3: 1 M ratio of MAI to total metal acetate content to afford a clear solution at 70 °C. Iron(II) acetate precursor ($Fe(OAc)_2$) was used due to the poor solubility of FeI_2 in DMF. By varying the incorporated concentration of Fe^{2+} in $MAPbI_3$, color changes were clearly observed in corresponding precursor solutions, as shown in Fig. S1. All perovskite precursor solutions were filtered with a 0.45 μm PVDF filter prior to use.

2.4. Fabrication of a $MAPb_{1-x}Fe_xI_3$ PEG

All device fabrication processes were performed under ambient air and room-temperature conditions. For device fabrication, ITO-coated PET substrates were ultrasonically cleaned with acetone, methanol and isopropyl alcohol for 20 min and rinsed with deionized water. The substrates were treated with oxygen plasma for 10 min to remove any organic residues. The perovskite precursor solution (70 μl) was spin-coated onto the substrate at 1000 rpm and 3500 rpm for 10 and 25 s, respectively. During the spin-coating at 3500 rpm, 200 μl of toluene (anti-solvent) was quickly dropped onto the substrate to induce the growth of the perovskite film. Finally, the perovskite film was washed with isopropyl alcohol to remove the excess MAI and spun at 3500 rpm for another 20 s. All the spin-coated films were annealed at 70 °C under ambient air for 10 min on a hotplate, and further annealed at 90 °C for 1 h using rapid thermal annealing (RTA) under an ambient atmosphere of argon. The polydimethylsiloxane (PDMS) was spin-coated onto the Au/Ti-coated PI substrate, and Au (100 nm)/Ti (10 nm) as a top electrode was deposited by direct current (dc) sputtering on the PI (thickness ~ 36 μm) substrate. Finally, the PDMS-coated $MAPb_{1-x}Fe_xI_3$ films were stacked with a PDMS-Au/Ti/PI substrate, and cured at room temperature. For a poled-PEG device, the perovskite thin films were polled with various applied electric fields in order to align the polarization domains followed by a stack of PDMS-Au/Ti-PI as a top electrode with PDMS. Last, the top and bottom electrodes were wired with copper wires using conducting silver paste and finally glued with an epoxy resin. The size and active area of the $MAPb_{1-x}Fe_xI_3$ PEGs were $2 \times 2\ cm^2$ and $1 \times 1\ cm^2$, respectively.

2.5. Characterization and measurements

The morphology and thickness of the films were characterized via field-emission scanning electron microscopy (FE-SEM, TOPCON DS-130C). The crystallinity and phase changes of the $MAPb_{1-x}Fe_xI_3$ films with incorporated concentrations of Fe^{2+} were investigated by X-ray diffraction (Rigaku D/MAX-RC) using Cu Kα radiation (λ = 1.5406 Å). The phase transition analysis of $MAPb_{1-x}Fe_xI_3$ films for each incorporated concentration of Fe^{2+} was carried out via high-temperature XRD at 40 kV and 300 mA using Cu Kα radiation (λ = 1.5406 Å) at temperatures ranging from 23 to 80 °C in intervals of 3 °C at a heating rate of 1 °C/min. Ultraviolet-visible (UV–vis) absorption and photoluminescence (PL) spectra were measured using a SCINCO S-3100 spectrophotometer and an F-380 fluorescence spectrometer at room temperature, respectively. For the UV–vis absorbance and PL spectra, PMMA passivation was coated onto a $MAPb_{1-x}Fe_xI_3$/glass. The dielectric and leakage current properties were measured at room temperature using HP4194A impedance gain-phase and HP4194B semiconductor-parameter analyzers, respectively. The polarization-electric field (P-E) hysteresis curves of $MAPb_{1-x}Fe_xI_3$ films were determined at room temperature using a RT66A ferroelectric tester (Radiant Technology), operated in virtual ground mode. Here, Au was deposited onto $MAPb_{1-x}Fe_xI_3$/FTO by dc sputtering. The Au top electrode had an area of $50 \times 50\ \mu m^2$ and a thickness of 100 nm. We conducted the piezoresponse force microscopy (PFM) imaging using an atomic force microscope (MFP-3D Origin, Asylum Research) with a Pt/Ir-coated tip (EFM, NanoWord). We used dual ac resonance tracking PFM (DART-PFM) mode to scan the area of interest at a scan rate of 0.5 Hz. During the scans, we applied ac drive amplitude of 1.5 V at the frequencies of 328 kHz and 336 kHz to the tip and 1 V to the bottom electrode of the sample to remove the internal field to get a stable resonance behavior.

We measured the piezoresponse hysteresis loops by DART-PFM mode at 4 different points for 10 times at each point. We used pulse dc mode with ac bias voltage of 3 V and 332 kHz to the tip while sweeping the voltage pulses with width of 100 ms from 0, 6, 0, −6–0 V over 40 s. We repeated it for four times and averaged them. The amplitude and piezoresponse was adjusted by the quality factor based on a simple

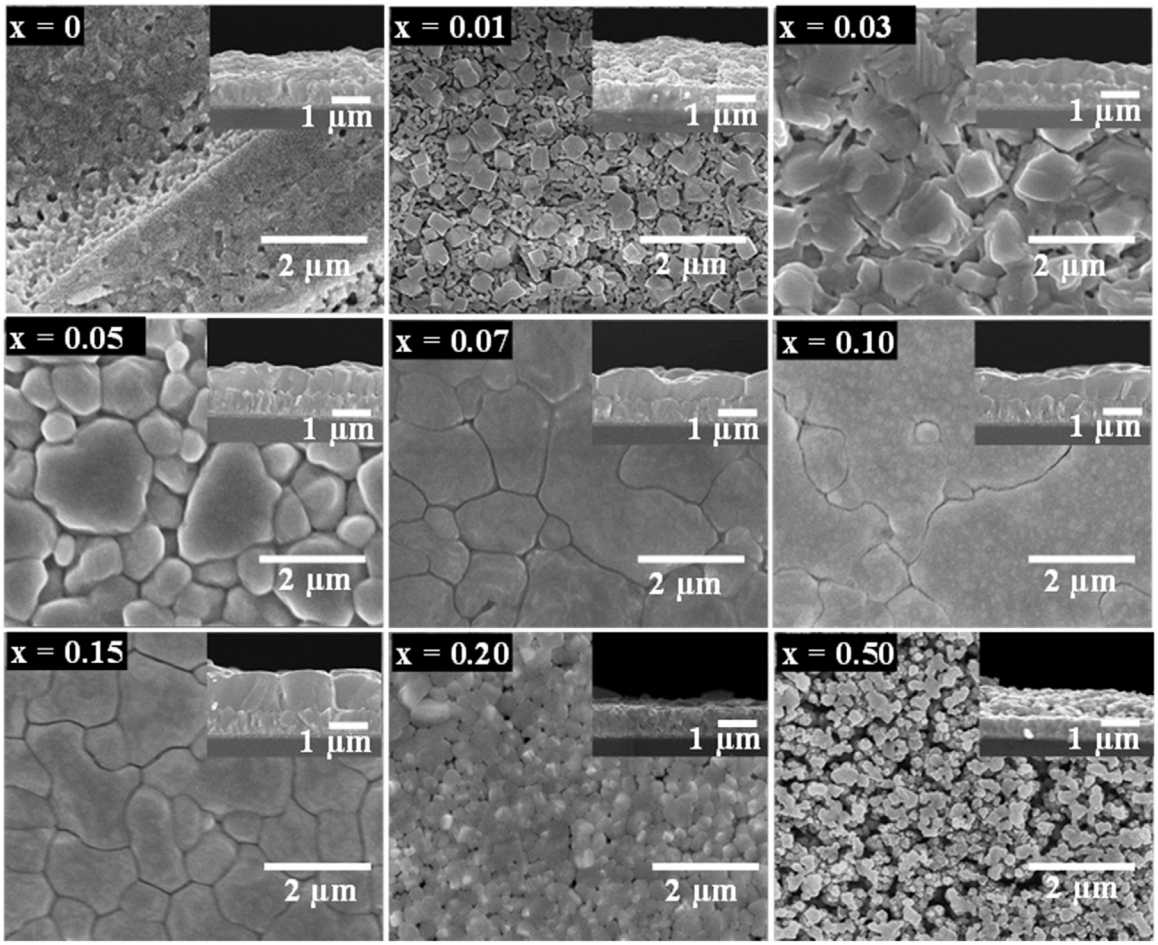

Fig. 1. SEM surface images; insets shoe cross-sectional images for different incorporated concentrations of Fe^{2+} in $MAPb_{1-x}Fe_xI_3$ thin films.

harmonic oscillator model to calibrate the amplitude because the amplitude is amplified by the resonance.

To monitor output performance, the fabricated PEG was placed on a custom-design mechanical system, where a periodical mechanical pressure was applied normal to the PEG via pushing and releasing modes. The input force on the PEG was instantly monitored by a load cell (Dacell UU-K20) during measurement. A digital oscilloscope (DSO1024A, Agilent Technologies) and a low-noise current amplifier (SR570, Stanford Research Systems) were used to record the output performance of PEGs.

3. Results and discussion

Fig. 1 shows the surface morphology and inset cross-section images of the $MAPb_{1-x}Fe_xI_3$ perovskite films with incorporating concentrations of Fe^{2+} ranging from x = 0–0.50. The thickness of the $MAPb_{1-x}Fe_xI_3$ ($0 \leq x \leq 0.50$) films was approximately 1 μm. Morphological variations were clearly observed in both the pristine and the Fe^{2+}-incorporated $MAPbI_3$ films. As the concentration of Fe^{2+} ($x \leq 0.10$) increased, the grain size of the films also noticeably increased. In addition to changes in the grain size, the morphology of the films became dense and uniform with no pinholes over the entire substrate. Higher incorporated concentrations of Fe^{2+} ($x \geq 0.15$), however, led to a reduction in grain size with numerous pinholes. Morphologically, the $MAPbI_3$ perovskite films tolerated incorporated levels of Fe^{2+} ions below x = 0.15 in a precursor solution. In particular, the incorporated levels of Fe^{2+} ($x \geq 0.20$) revealed negative impacts on the surface morphology such as a decrease in grain size and the development of pinholes and cracks. Therefore, the incorporated concentration of Fe^{2+} strongly influenced the crystalline size and quality of $MAPb_{1-x}Fe_xI_3$ films. High-quality $MAPb_{1-x}Fe_xI_3$ (x = 0.07 and 0.10) films are compacted with grain sizes of more than 2 μm, which translates to good electrical properties.

The UV–vis absorption spectra of $MAPbI_3$ films with different Fe^{2+} concentrations are illustrated in Fig. S2a. The optical band gap of the pristine $MAPbI_3$ films was 1.6 eV, which is in good agreement with the reported values (1.55–1.61 eV) [28]. By contrast, $MAPb_{1-x}Fe_xI_3$ ($0.01 \leq x \leq 0.50$) films displayed a blue shift in band gap energies (E_g) and the estimated E_g increased from 1.61 to 1.73 eV as Fe^{2+} concentration increased, which is consistent with previous reports [29]. In Fig. S2b, the steady-state photoluminescence (PL) spectra of pristine and $MAPb_{1-x}Fe_xI_3$ films show stable emission peaks with a blue shift in E_g with increases in Fe^{2+} concentration, which is in good agreement with the behavior of UV–vis absorption spectra. The blue shift in E_g with increasing Fe^{2+} clearly indicated the formation of $MAPb_{1-x}Fe_xI_3$ via partial replacement of Pb^{2+} with Fe^{2+} in $MAPbI_3$.

Fig. 2a illustrates the X-ray diffraction patterns of $MAPb_{1-x}Fe_xbI_3$ ($0 \leq x \leq 0.50$) films and the enlarged XRD patterns, which were measured at room temperature. All the diffraction peaks of $MAPb_{1-x}Fe_xbI_3$ ($0 \leq x \leq 0.50$) films were similar to that of a pristine $MAPbI_3$ XRD pattern with a small shift in the peak position, while the extra peak at $2\theta = 11.6^\circ$ for Fe^{2+} (x = 0.50) may represent the formation of intermediate or complex phases such as PbI_2-MAI-DMF, $MAPbI_3$·DMF, or $MAPbI_3{\cdot}2H_2O$ [30,31]. Figs. 2b and 2c clearly show the two strongest diffraction peaks at $2\theta = 14.1^\circ$ and 28.6°, respectively. As the incorporated concentration of Fe^{2+} increased, the peaks of $MAPb_{1-x}Fe_xI_3$ films were uniformly shifted toward diffraction angles that were lower than those of pristine $MAPbI_3$, which all have tetragonal structures at

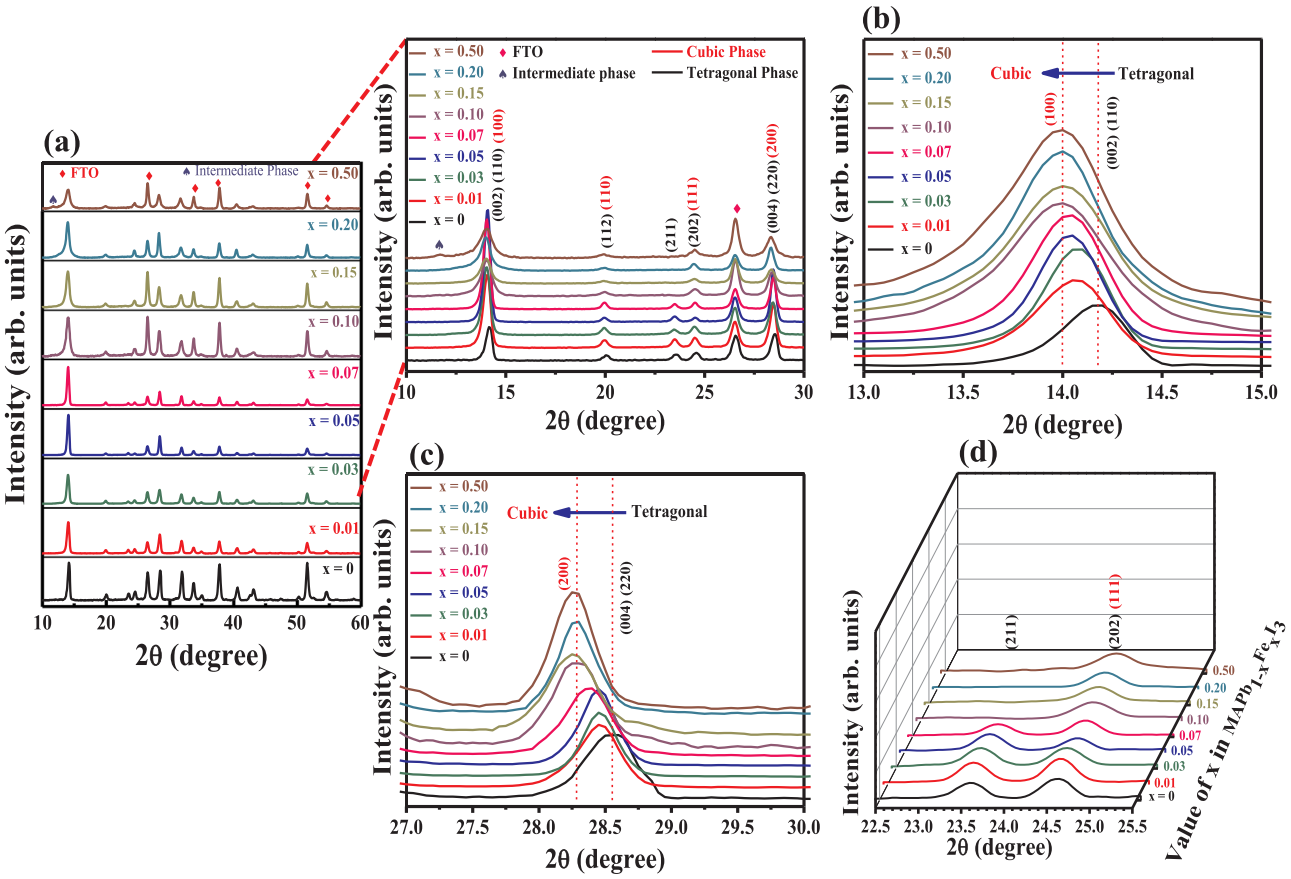

Fig. 2. (a) XRD patterns of $MAPb_{1-x}Fe_xI_3$ ($0 \le x \le 0.50$) films deposited onto a FTO substrate and its XRD pattern enlarged in a range of 2θ = 10–30° measured at room temperature with different Fe^{2+} concentrations. The enlarged XRD patterns for a 2θ range of (b) 13–15°, (c) 27–30°, and (d) 22.5–25.5°, respectively.

room temperature [32]. In Fig. 2d, the disappearance of the (211) and (202) planes at $2\theta = 23.6°$ and 24.6° respectively, and the occurrence of a new (111) plane at $2\theta = 24.1°$ indicated the phase transition from tetragonal to cubic with a change in the incorporated concentration of Fe^{2+} ($x \ge 0.10$) when compared with the simulated XRD pattern of $MAPbI_3$ [33]. Therefore, $MAPb_{1-x}Fe_xI_3$ perovskite with the partial replacement of Pb^{2+} with Fe^{2+} ($x \le 0.07$) had a tetragonal structure, and the heavy incorporation of Fe^{2+} ($x > 0.07$) led to a phase transformation from a tetragonal to a cubic structure. The transition from a tetragonal to a cubic phase was confirmed between x = 0.07–0.10 for an incorporated concentration of Fe^{2+}.

The Fe^{2+} ion can be easily incorporated into $MAPbI_3$ structure because the ionic radius of Fe^{2+} (0.78 Å) is smaller than that of Pb^{2+}(1.19 Å). The stability and transformation of tetragonal to cubic phase of Fe-incorporated $MAPbI_3$ can be understood in terms of the geometric tolerance factor *t*, that was defined as $(R_{MA}+R_I)/(\sqrt{2}(R_{Pb/Fe}+R_I))$. The tolerance factor of $MAPbI_3$ is 0.85, whereas it is 0.85–0.90 for $MAPb_{1-x}Fe_xI_3$ ($0.01 \le x \le 0.50$), which is depended on the incorporating concentration. In particular, the tolerance factor for the Fe^{2+}(x = 0.07) is 0.85, whereas it is 0.86 for x = 0.10. Therefore, the more incorporation of Fe^{2+} into $MAPbI_3$, the higher tolerance factor that is. From the reported literature, the lead halide perovskites have the tolerance factor in the range of $0.84 < t < 0.86$ [34,35]. Therefore, the tolerance factor of $MAPb_{1-x}Fe_xI_3$ ($0.01 \le x \le 0.07$) is within the range of $MAPbI_3$ tolerance factor. However, above the doping level of Fe^{2+} ($x \ge 0.10$) leads structural distortion results in tetragonal to cubic phase transition as observed in our experimental results. Therefore, it is revealed that the critical composition of Fe^{2+} in $MAPb_{1-x}Fe_xI_3$ was located between 0.07 and 0.10.

XRD at variable high temperatures was used to investigate the incorporation (Fe^{2+}) effect on the tetragonal-cubic phase transition of $MAPb_{1-x}Fe_xI_3$ films with incorporating $x \le 0.07$, since the $MAPb_{1-x}Fe_xI_3$ films showed a cubic structure above an incorporated level of Fe^{2+} ($x > 0.07$). The magnified peaks and temperature-dependent XRD patterns of $MAPb_{1-x}Fe_xI_3$ ($0.01 \le x \ge 0.50$) films are shown in Figs. S3-S6. The strong diffraction peaks at $2\theta = 14.1°$ and 28.6° in the magnified XRD pattern clearly depict a peak shift to a lower angle position as a function of temperature increases from room temperature to 341 K in intervals of 3 K. According to Baikie *et al.*, the disappearance of (211) and the evolution of the (111)/(202) plane obviously indicates the formation of a cubic structure [36], and the same trend appears in Figs. S3-S6 for each incorporated concentration of Fe^{2+} at different measurement temperatures. The tetragonal-to-cubic phase-transition temperatures for various incorporated concentrations of $MAPb_{1-x}Fe_xI_3$ films are given in Fig. 3. The estimated tetragonal-to-cubic transition temperature of $MAPb_{1-x}Fe_xI_3$ (x = 0.01) film with a lower level of Fe^{2+} incorporating was approximately 329–332 K (~ 56–59 °C), which is similar to the tetragonal-to-cubic phase transition temperature (~ 330 K) of $MAPbI_3$ [37]. As the incorporated concentrations of Fe^{2+} increased from x = 0.01–0.07, the transition temperature also decreased and reached a final value between 317 and 320 K (~ 44–47 °C). Based on the XRD results measured at both room and high temperature, the $MAPb_{1-x}Fe_xI_3$ films remained in the tetragonal phase at an incorporating level of x = 0.07. The estimated average transition temperatures were 57.5, 54.5, 49.5, and 45.5 °C with a ± 1.5 error range for incorporating concentrations of x = 0.01, 0.03, 0.05, and 0.07, respectively.

Fig. 4a and 4b shows the variations in the frequency dependent dielectric constant (ε_r) and the dissipation factor of $MAPb_{1-x}Fe_xI_3$ ($0 \le x \le 0.50$) films at room temperature respectively. The dielectric constant of pristine $MAPbI_3$ films was ~ 47 at 100 kHz, which is comparable to a previously published dielectric constant report

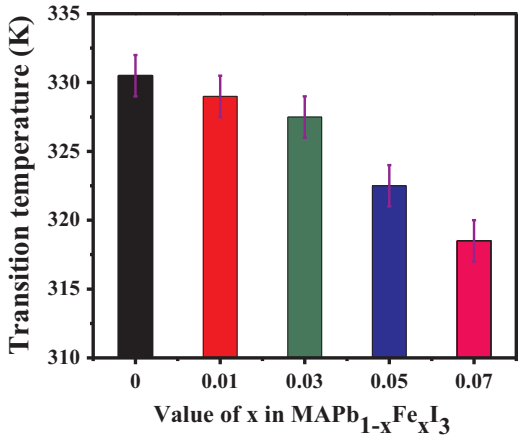

Fig. 3. Variations in the phase-transition temperature of $MAPb_{1-x}Fe_xI_3$ ($0 \le x \le 0.07$) films as a function of the Fe^{2+} incorporated concentration.

(x = 0.10) film from a ferroelectric to a paraelectric phase. Because the ionic radius of the incorporated Fe^{2+} is smaller than that of the Pb^{2+}, when the critical amount of the Fe^{2+} ($x \le 0.07$) was incorporated into the sites of the Pb^{2+}, the lattice of the $MAPbI_3$ has a high residual stress, which increases the grain size to relieve the stress during the crystalline process. The large grain size increased the dielectric constant of the Fe^{2+} incorporated-$MAPbI_3$ films below x = 0.07 (ferroelectric property with tetragonal structure).

Fig. 4d shows the field dependence of the leakage current density for $MAPb_{1-x}Fe_xI_3$ ($0 \le x \le 0.50$) films. The leakage current density of all the films progressively increased with increases in the applied field. The leakage current density of the $MAPbI_3$ films was approximately 10^{-5} A/cm^2 at 10 kV/cm. As the applied field was increased to 50 kV/cm, the leakage current density suddenly increased to 10^{-2} A/cm^2. By contrast, the leakage current densities of $MAPb_{1-x}Fe_xI_3$ (x = 0.07 and 0.10) films were increased with increasing the electric field from 0 to 50 kV/cm. However, leakage current densities were less than ~ μA/cm^2 at 50 kV/cm. The leakage current density of the films was decreased

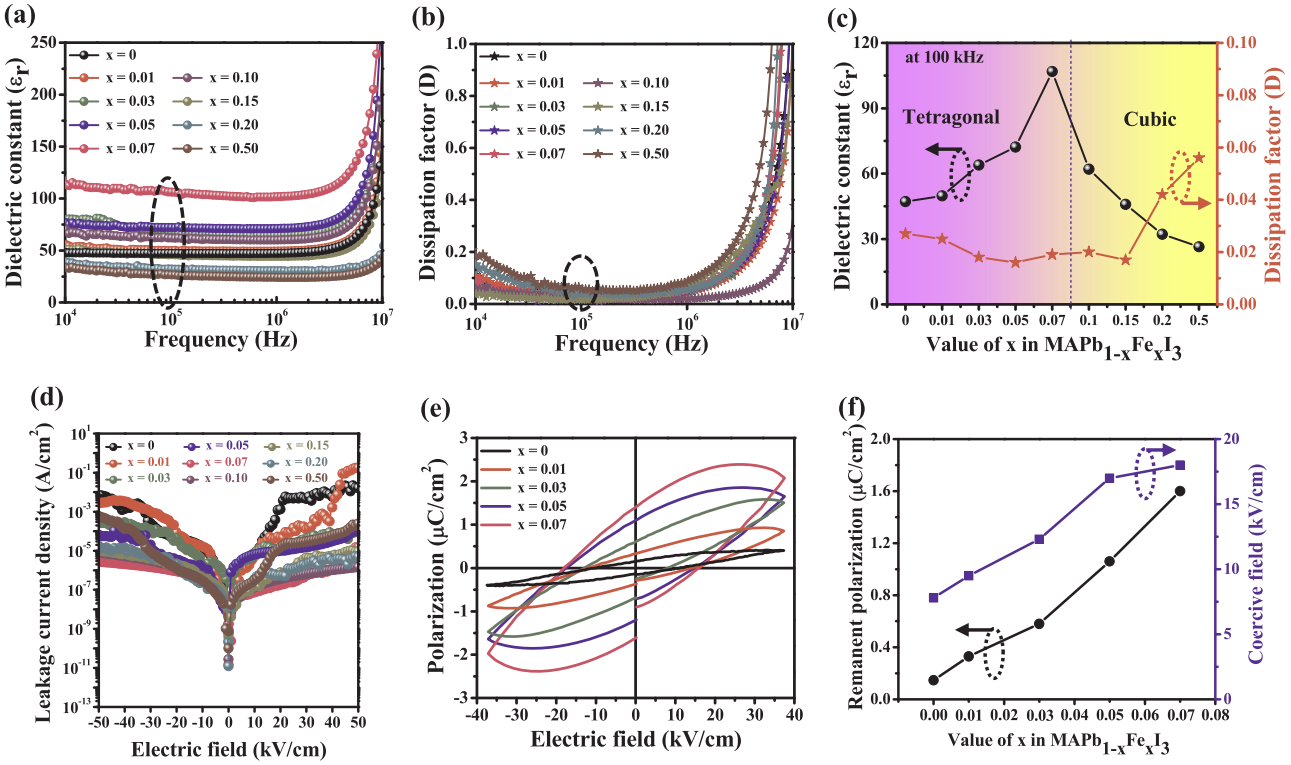

Fig. 4. (a) Dielectric constant and (b) dissipation factor of $MAPb_{1-x}Fe_xI_3$ ($0 \le x \le 0.50$) thin films as a function of frequency at room temperature. (c) Variations in dielectric constant and dissipation factor of $MAPb_{1-x}Fe_xI_3$ ($0 \le x \le 0.50$) films with different incorporated concentrations of Fe^{2+}. (d) Leakage current density vs. applied electric field for $MAPb_{1-x}Fe_xI_3$ ($0 \le x \le 0.50$) films at room temperature. (e) Polarization-electric field (P-E) curves of $MAPb_{1-x}Fe_xI_3$ ($0 \le x \le 0.07$) films. (f) Remanent polarization (P_r) and coercive field (E_r) of $MAPb_{1-x}Fe_xI_3$ ($0 \le x \le 0.07$) thin films as a function of Fe^{2+} incorporated concentration.

[27,38]. With increases in the incorporated (Fe^{2+}) concentration in $MAPbI_3$ films, the dielectric constant was remarkably increased to a maximum value of $\varepsilon_r \sim 107$ at x = 0.07, but was decreased rapidly thereafter with further increases in the incorporated concentrations of Fe^{2+} ($x \ge 0.10$). As shown in Fig. 4b, there is a low dissipation factor (~ 0.03) for $MAPb_{1-x}Fe_xI_3$ ($0 \le x \le 0.15$) films, which validates the reliability of obtained dielectric constants, whereas the samples for incorporated concentrations of x = 0.20 and 0.50 exhibited slightly high dissipation factors due to the low quality of the films (Fig. 1). Fig. 4c clearly shows the discrepancies in the dielectric constant and dissipation factors of $MAPb_{1-x}Fe_xI_3$ ($0 \le x \le 0.50$) films measured as a function of Fe^{2+} concentration when observed at a frequency of 100 kHz. These results demonstrate the transition of $MAPb_{1-x}Fe_xI_3$ with increases of the Fe^{2+} concentration from x = 0.01–0.10, after which leakage current densities were increased with further increases above x = 0.10. These results reveal that the incorporation of small amounts of Fe^{2+} (x = 0.07 and 0.10) leads to a marked improvement in leakage current density. Fig. 4e illustrates the ferroelectric *P-E* hysteresis loops of $MAPb_{1-x}Fe_xI_3$ ($0 \le x \le 0.07$) films at room temperature. These films exhibited the typical *P-E* hysteresis loops even in a high applied electric field of 40 kV/cm. The remanent polarization (P_r) and coercive field (E_c) of the $MAPb_{1-x}Fe_xI_3$ films and incorporated concentrations of Fe^{2+} ($x \le 0.07$) are depicted in Fig. 4f. The remanent polarization of the films steadily increased with increases in the Fe^{2+} content, while a large remanent polarization of 1.6 μC/cm^2 and a coercive field of 18 kV/cm were obtained for incorporating with Fe^{2+}

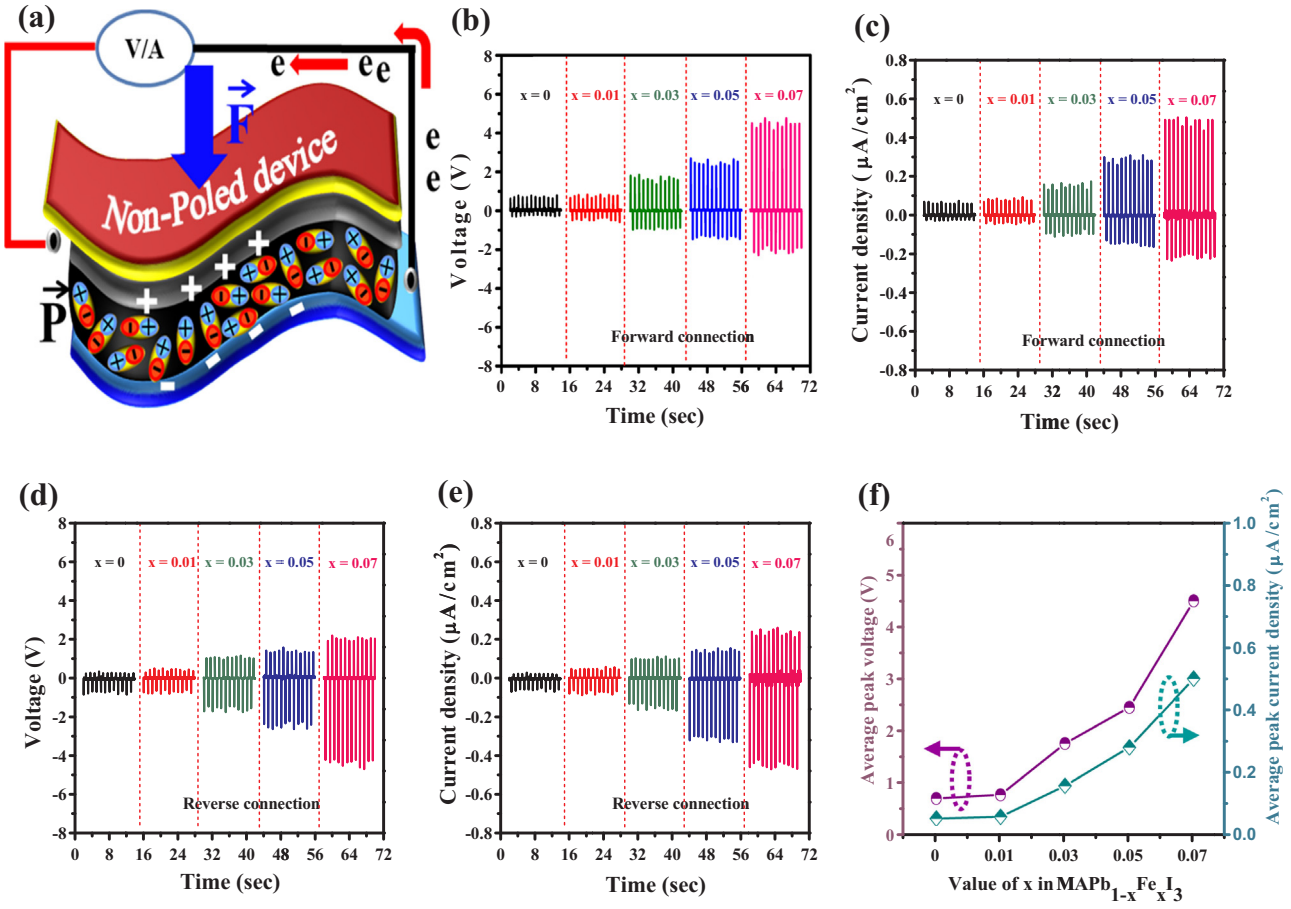

Fig. 5. (a) Schematic diagram for the power generation mechanism of non-poled $MAPb_{1-x}Fe_xI_3$ ($0 \le x \le 0.07$) film-based PEGs. Output voltage and current density of $MAPb_{1-x}Fe_xI_3$ ($0 \le x \le 0.07$) PEGs measured by forward connection of (b) and (c), and reverse connection of (d) and (e), respectively. (f) Comparison of the average peak output voltage and current density as a function of Fe^{2+} incorporated concentration.

($x = 0.07$) at an applied electric field of 35 kV/cm.

PFM imaging was performed to analyze the piezoelectric properties of the $MAPb_{1-x}Fe_xI_3$ ($x = 0.07$) films using DART-PFM mode (Fig. S7). The effective d_{33} piezoelectric coefficient of the $MAPb_{1-x}Fe_xI_3$ ($x = 0.07$) films was evaluated by averaging the piezoresponse amplitude divided by the quality factor and ac bias voltage of 3 V. The effective d_{33} piezoelectric coefficient was approximately $17.0 \pm 6.0\ pm\ V^{-1}$, which was higher than that ($5.12\ pm\ V^{-1}$) of $MAPbI_3$ films [27].

Fig. 5a shows a schematic of the piezoelectric power generation mechanism for a nonpoled $MAPb_{1-x}Fe_xI_3$ ($0 \le x \le 0.07$) PEG. The fabrication steps for a $MAPb_{1-x}Fe_xI_3$ ($0 \le x \le 0.07$) film-based PEG are clearly plotted in Fig. S8a, and details of the fabrication procedure are discussed in the experimental section. Fig. S8b shows the captured image of the fabricated PEG being bent with fingers, which indicates good flexibility/suitability for wearable electronic applications. When a non-poled PEG is subjected to a mechanical pressure, the mechanical stress can induce relatively small piezoelectric charges due to randomly oriented polarization domains, which results in a potential difference in both the top and bottom electrodes. Figs. 5b and 5c show the periodic application of mechanical pressure in vertical pressing and releasing modes using a force simulator and the generation of piezoelectric output voltage and output current for non-poled $MAPb_{1-x}Fe_xI_3$ ($0 \le x \le 0.07$) PEGs. Here, all the fabricated PEGs were measured under a mechanical stress of 0.5 MPa at a frequency of 1 Hz using an active area of $1 \times 1\ cm^2$. The values for output voltage and current density for a pristine $MAPbI_3$ PEG were 0.72 V and 0.056 μA/cm², respectively, which is consistent with the reported values for non-poled $MAPbI_3$ thin-film PEGs [27]. With increases in the Fe^{2+} concentration in $MAPb_{1-x}Fe_xI_3$ ($0.01 \le x \le 0.07$), the average peak output voltage and output current density increased in a linear fashion and reached maximum values of ~ 4.52 V and 0.50 μA/cm² at $x = 0.07$. These results suggest that the dielectric constant (~107) of $MAPb_{1-x}Fe_xI_3$ ($x = 0.07$) strongly influences the generation of piezoelectric potential as well as piezoelectric polarization, which enhances the piezoelectric output performance. To confirm the validation of output signals, a switching polarity test was carried out using all the fabricated devices. Negative output signals were obtained with a reverse connection of PEGs, and the amplitudes of output signals were almost equal to those obtained with a forward connection, as shown in Figs. 5d and 5e. The averages for the peak output voltages and current densities of $MAPb_{1-x}Fe_xI_3$ ($0 \le x \le 0.07$) PEGs as a function of incorporated (Fe^{2+}) concentration are summarized in Fig. 5f. The output voltages and current densities increased in a linear fashion with increases of Fe^{2+} concentration, and the $MAPb_{1-x}Fe_xI_3$ ($x = 0.07$) PEG showed values that were 6.2 times higher than that of a pristine $MAPbI_3$ PEG. The output performance of a non-poled $MAPb_{1-x}Fe_xI_3$ ($x = 0.07$) PEG was also measured in both forward and reverse connection under applied mechanical pressures that varied from 0.1 to 0.5 MPa, as shown in Fig. S9a-d. An applied mechanical pressure of 0.5 MPa significantly increased the maximum output performance of the PEG.

Fig. 6a shows a schematic representation of the piezoelectric power generation mechanism for a poled-$MAPb_{1-x}Fe_xI_3$ ($x = 0.07$) PEG, because a non-poled $MAPb_{1-x}Fe_xI_3$ ($x = 0.07$) PEG showed an output performance that was higher than that of other concentrations of Fe^{2+}. The output voltages and current densities of poled devices for different

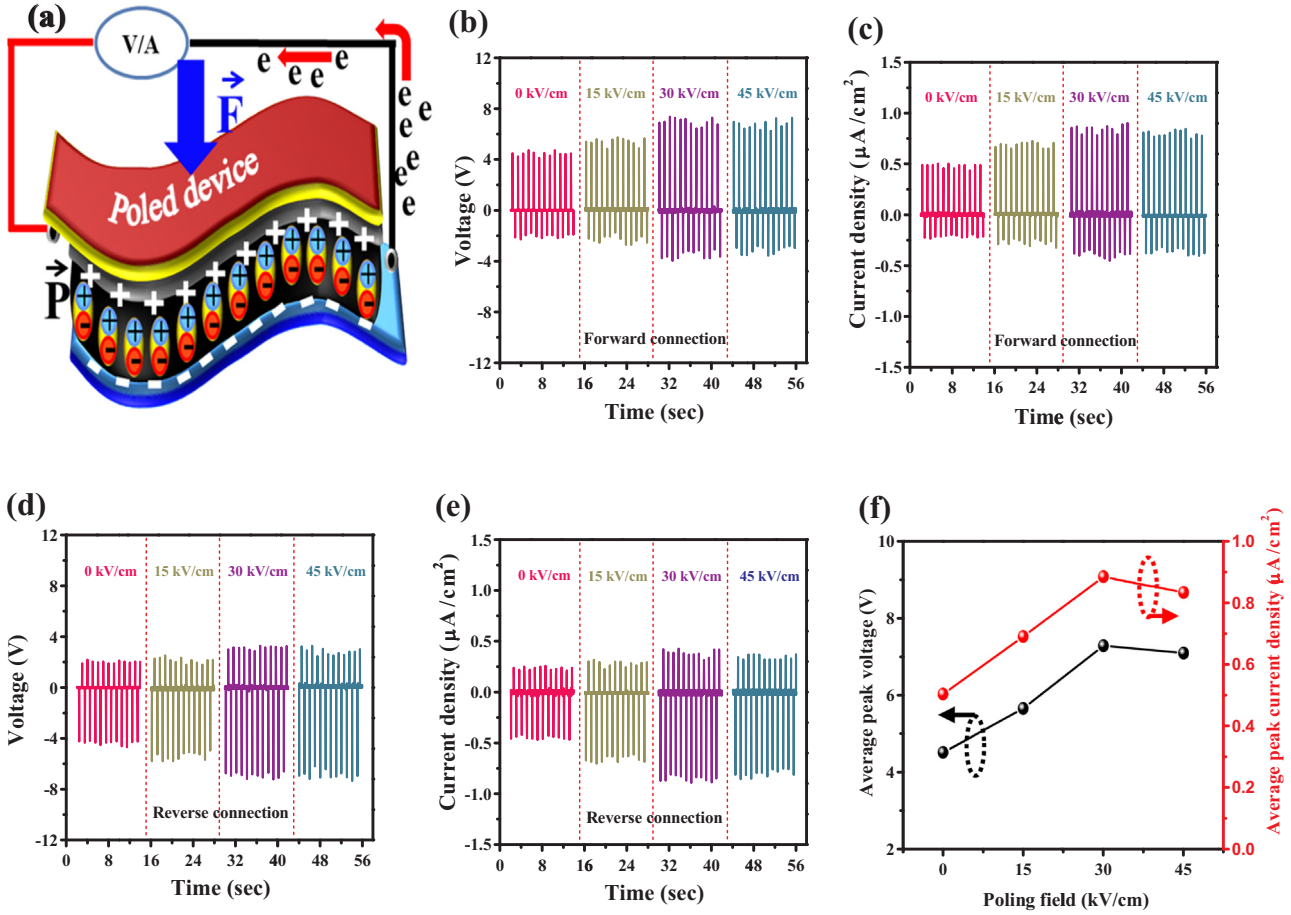

Fig. 6. (a) Schematic diagram for the power generation mechanism of poled $MAPb_{1-x}Fe_xI_3$ (x = 0.07) film-based PEGs. Output voltage and current density of poled $MAPb_{1-x}Fe_xI_3$ (x = 0.07) PEGs measured by forward connection of (b) and (c), and reverse connection of (d) and (e), respectively. (f) Comparison of average peak output voltage and current density measured under various applied poling fields using $MAPb_{1-x}Fe_xI_3$ (x = 0.07) PEGs.

poling fields at an applied mechanical pressure of 0.5 MPa are shown in Figs. 6b and 6c, respectively. The poled devices exhibited an enhancement in output performance of as much as 30 kV/cm when compared with non-poled versions, and showed saturation at 45 kV/cm. The switching of polarity was observed for devices, and Figs. 6d and 6e clearly show the output signals switched in reverse connection. These results confirmed that the obtained output signals originate from the piezoelectric properties. Fig. 6f illustrates variations in the average peak voltage and current density of the generator as a function of the poling field, and the output performance progressively increased until the poling field reached 30 kV/cm. The maximum values for output voltage and current density of $MAPb_{1-x}Fe_xI_3$ (x = 0.07) were ~ 7.29 V and 0.88 μA/cm^2, respectively, for a poling field of 30 kV/cm, which represents a 1.6-fold improvement over non-poled devices incorporated with Fe^{2+} (x = 0.07). The variations in average peak voltage and current density for a $MAPb_{1-x}Fe_xI_3$ (x = 0.07) PEG with a poling field of 30 kV/cm as a function of applied mechanical pressure are shown in Fig. S10.

To demonstrate the practical application of a PEG, the $MAPb_{1-x}Fe_xI_3$ (x = 0.07)-based PEG was connected to a commercial LED using a bridge rectifier consisting of four diodes (Fig. 7c), which converts the generated output from AC to DC signals. Figs. 7a and 7b show the rectified output voltage and current density, respectively, which were sufficient to power a commercial LED without the aid of a capacitor since the operation voltage of a commercial red LED is ~ 2 V. The instant lightening of the LED using generated power from a PEG without a storage device is shown in Fig. 7d (the instant lightning was shown in Supplementary video file).

Supplementary material related to this article can be found online at http://dx.doi.org/10.1016/j.nanoen.2018.04.031.

A durability test also was performed with a poled $MAPb_{1-x}Fe_xI_3$ (x = 0.07) PEG to confirm its mechanical endurance under vertical pressing and releasing modes using an applied mechanical pressure of 0.5 MPa. The obtained output signals of more than 600 cycles are shown in Fig. 7e (output voltage) and Fig. 7f (output current density). The enlarged output signals in each inset show voltage and current density values of approximately 7.1 V and 0.85 μA/cm^2, respectively. These output signals of the PEG were relatively stable even after 600 cycles. In addition, we performed these measurements using multiple devices for two weeks, and observed no degradation in performance, which confirms the reproducibility and stability of a $MAPb_{1-x}Fe_xI_3$ (x = 0.07) PEG device.

4. Conclusions

In summary, we have systematically investigated the effect that the incorporated concentration of Fe^{2+} can exert on the structural, electrical, dielectric, and piezoelectric properties of $MAPbI_3$ films. The partial replacement of Pb^{2+} with Fe^{2+} in $MAPbI_3$ perovskite films significantly improved both morphology and crystallinity. The replacement of Pb^{2+} with Fe^{2+} changed the structure from tetragonal to cubic, and it also changed the temperatures for the phase transition of $MAPb_{1-x}Fe_xI_3$. As the Fe^{2+} concentration was increased in $MAPb_{1-x}Fe_xI_3$ ($0 \le x \le 0.07$), the dielectric constant increased from ~ 47 to 107 at 100 kHz. In particular, $MAPb_{1-x}Fe_xI_3$ (x = 0.07) films showed a high dielectric constant of ~ 107 and a tetragonal-cubic transition

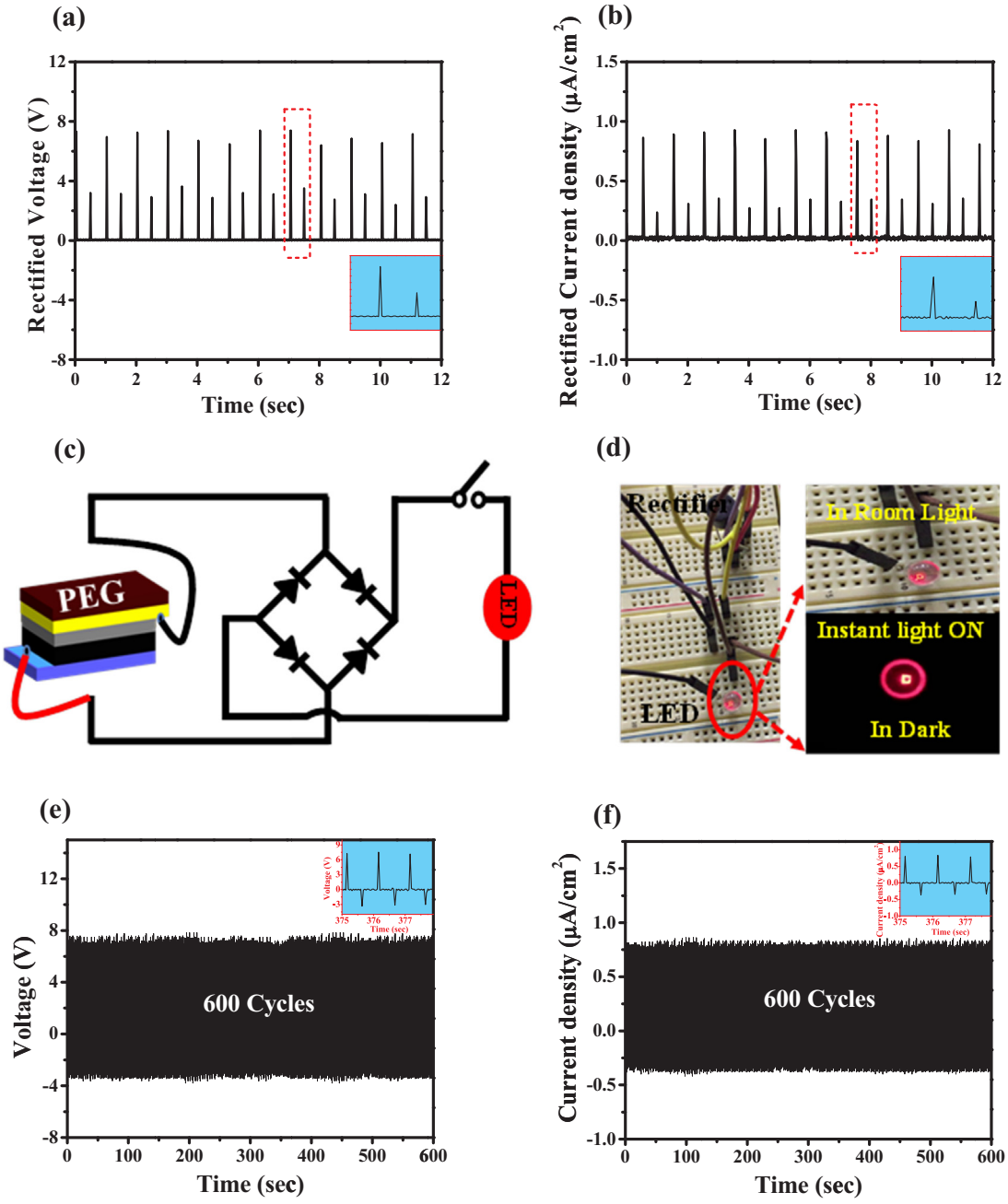

Fig. 7. Rectified output voltage (a) and current density (b) of poled $MAPb_{1-x}Fe_xI_3$ (x = 0.07) PEGs; insets show enlarged signals from the dashed lines. (c) Schematic rectifying circuit diagram of PEGs for powering the LED. (d) Captured image of the instant LED light on during applied mechanical pressure. Cyclic output voltage (e) and current density (f) for 600 cycles; insets show magnified signals.

temperature of ~ 45.5 ± 1.5 °C. The high dielectric constant for $MAPb_{1-x}Fe_xI_3$ ($0 \le x \le 0.07$) films enhanced the piezoelectric output performance of the PEGs. The values for output voltage and current density of poled $MAPb_{1-x}Fe_xI_3$ (x = 0.07) PEGs with a poling field of 30 kV/cm were approximately 7.29 V and 0.88 μA/cm^2, which was much higher than either non-poled $MAPb_{1-x}Fe_xI_3$ (x = 0.07) or the values reported for $MAPbI_3$-based PEGs. The enhanced output power of the poled $MAPb_{1-x}Fe_xI_3$ (x = 0.07) generator was sufficient to instantly light a commercial LED. This innovative approach to the structural modification of organic-inorganic perovskite materials by replacing/substituting with different elements could further the development of a wide range of wearable energy harvesters for use in portable, self-powered, electronic devices.

Acknowledgements

This work was supported by a National Research Foundation of Korea (NRF) grant funded by the Korean government (MSIP) (No. NRF-2013R1A4A1069528) and was partially supported via Creative Materials Discovery Program from National Research Foundation of Korea funded by the Ministry of Science and ICT (NRF-2017M3D1A1086861).

Appendix A. Supporting information

Supplementary data associated with this article can be found in the online version at http://dx.doi.org/10.1016/j.nanoen.2018.04.031.

References

[1] M.P. Lumb, S. Mack, K.J. Schmieder, M. González, M.F. Bennett, D. Scheiman, M. Meitl, B. Fisher, S. Burroughs, K.-T. Lee, J.A. Rogers, R.J. Walters, GaSb-based solar cells for full solar spectrum energy harvesting, Adv. Energy Mater. 7 (2017) 1700345.

[2] S.J. Kim, H.E. Lee, H. Choi, Y. Kim, J.H. We, J.S. Shin, K.J. Lee, B.J. Cho, High-performance flexible thermoelectric power generator using laser multiscanning lift-off process, ACS Nano 10 (2016) 10851–10857.

[3] Z.L. Wang, J. Chen, L. Lin, Progress in triboelectric nanogenerators as a new energy technology and self-powered sensors, Energy Environ. Sci. 8 (2015) 2250–2282.

[4] K.I. Park, J.H. Son, G.T. Hwang, C.K. Jeong, J. Ryu, M. Koo, I. Choi, S.H. Lee, M. Byun, Z.L. Wang, K.J. Lee, Highly-efficient, flexible piezoelectric PZT thin film nanogenerator on plastic substrates, Adv. Mater. 26 (2014) 2514–2520.

[5] H.V. Ngoc, D.J. Kang, Flexible, transparent and exceptionally high power output nanogenerators based on ultrathin ZnO nanoflakes, Nanoscale 8 (2016) 5059–5066.

[6] C.-Y. Chen, G. Zhu, Y. Hu, J.-W. Yu, J. Song, K.-Y. Cheng, L.-H. Peng, L.-J. Chou, Z.L. Wang, Gallium nitride nanowire based nanogenerators and light-emitting diodes, ACS Nano 6 (2012) 5687–5692.

[7] J.M. Wu, C.C. Kao, Self-powered pendulum and micro-force active sensors based on a ZnS nanogenerator, RSC Adv. 4 (2014) 13882–13887.

[8] Y.F. Lin, J. Song, Y. Ding, S.-Y. Lu, Z.L. Wang, Piezoelectric nanogenerator using CdS nanowires, Appl. Phys. Lett. 92 (2008) 022105.

[9] W. Wu, S. Bai, M. Yuan, Y. Qin, Z.L. Wang, T. Jing, Lead zirconate titanate nanowire textile nanogenerator for wearable energy-harvesting and self-powered devices, ACS Nano 6 (2012) 6231–6235.

[10] S. Xu, Y.-W. Yeh, G. Poirier, M.C. McAlpine, R.A. Register, N. Yao, Flexible piezoelectric PMN–PT nanowire-based nanocomposite and device, Nano Lett. 13 (2013) 2393–2398.

[11] J.H. Jung, M. Lee, J. Hong, Y. Ding, C.-Y. Chen, L.-J. Chou, Z.L. Wang, Lead-free $NaNbO_3$ nanowires for a high output piezoelectric nanogenerator, ACS Nano 5 (2011) 10041–10046.

[12] S. Paria, S.K. Karan, R. Bera, A.K. Das, A. Maitra, B.B. Khatua, A facile approach to develop a highly stretchable PVC/$ZnSnO_3$ piezoelectric nanogenerator with nigh output power generation for powering portable electronic devices, Ind. Eng. Chem. Res. 55 (2016) 10671–10680.

[13] C. Chang, V.H. Tran, J. Wang, Y.-K. Fuh, L. Lin, Direct-write piezoelectric polymeric nanogenerator with high energy conversion efficiency, Nano Lett. 10 (2010) 726–731.

[14] X.L. Chen, H.M. Tian, X.M. Li, J.Y. Shao, Y.C. Ding, N.L. An, Y.P. Zhou, A high performance P(VDF-TrFE) nanogenerator with self-connected and vertically integrated fibers by patterned EHD pulling, Nanoscale 7 (2015) 11536.

[15] Y. Luo, I. Szafraniak, N.D. Zakharov, V. Nagarajan, M. Steinhart, R.B. Wehrspohn, J.H. Wendorff, R. Ramesh, M. Alexe, Nanoshell tubes of ferroelectric lead zirconate titanate and barium titanate, Appl. Phys. Lett. 83 (2003) 440–442.

[16] X. Chen, S. Xu, N. Yao, W. Xu, Y. Shi, Potential measurement from a single lead ziroconate titanate nanofiber using a nanomanipulator, Appl. Phys. Lett. 94 (2009) 253113.

[17] M.A. Green, A. Ho-Baillie, H.J. Snaith, The emergence of perovskite solar cells, Nat. Photonics 8 (2014) 506–514.

[18] R. Dong, Y. Fang, J. Chae, J. Dai, Z. Xiao, Q. Dong, Y. Yuan, A. Centrone, X.C. Zeng, J. Huang, High-gain and low-driving-voltage photodetectors based on organolead triiodide perovskites, Adv. Mater. 27 (2015) 1912–1918.

[19] Z.-K. Tan, R.S. Moghaddam, M.L. Lai, P. Docampo, R. Higler, F. Deschler, M. Price, A. Sadhanala, L.M. Pazos, D. Credgington, F. Hanusch, T. Bein, H.J. Snaith, R.H. Friend, Bright light-emitting diodes based on organometal halide perovskite, Nat. Nanotechnol. 9 (2014) 687–692.

[20] X.Y. Chin, D. Cortecchia, J. Yin, A. Bruno, C. Soci, Lead iodide perovskite light-emitting field-effect transistor, Nat. Commun. 6 (2015) 7383.

[21] H. Zhu, Y. Fu, F. Meng, X. Wu, Z. Gong, Q. Ding, M.V. Gustafsson, M.T. Trinh, S. Jin, X.-Y. Zhu, Lead halide perovskite nanowire lasers with low lasing thresholds and high quality factors, Nat. Mater. 14 (2015) 636–642.

[22] J. You, Z. Hong, Y. (M.) Yang, Q. Chen, M. Cai, T.-B. Song, C.-C. Chen, S. Lu, Y. Liu, H. Zhou, Y. Yang, Low-temperature solution-processed perovskite solar cells with high efficiency and flexibility, ACS Nano 8 (2014) 1674–1680.

[23] S.S. Shin, E.J. Yeom, W.S. Yang, S. Hur, M.G. Kim, J. Im, J. Seo, J.H. Noh, S.I. Seok, Colloidally prepared La-doped $BaSnO_3$ electrodes for efficient, photostable perovskite solar cells, Science 356 (2017) 167–171.

[24] H. Röhm, T. Leonhard, M.J. Hoffmann, A. Colsmann, Ferroelectric domains in methylammonium lead iodide perovskite thin-films, Energy Environ. Sci. 10 (2017) 950–955.

[25] S. Liu, F. Zheng, I. Grinberg, A.M. Rappe, Photoferroelectric and photopiezoelectric properties of organometal halide perovskites, J. Phys. Chem. Lett. 7 (2016) 1460–1465.

[26] M. Coll, A. Gomez, E.M. Marza, O. Almora, G. Garcia-Belmonte, M.C. Quiles, J. Bisquert, Polarization switching and light-enhanced piezoelectricity in lead halide perovskites, J. Phys. Chem. Lett. 6 (2015) 1408–1413.

[27] Y.J. Kim, T.V. Dang, H.J. Choi, B.J. Park, J.H. Eom, H.A. Song, D. Seol, Y. Kim, S.H. Shin, H. Nah, S.G. Yoon, Piezoelectric properties of $CH_3NH_3PbI_3$ perovskite thin films and their applications in piezoelectric generators, J. Mater. Chem. A 4 (2016) 756–763.

[28] C. Quarti, E. Mosconi, J.M. Ball, V. D'Innocenzo, C. Tao, S. Pathak, H.J. Snaith, A. Petrozza, F. De Angelis, Structural and optical properties of methylammonium lead iodide across the tetragonal to cubic phase transition: implications for perovskite solar cells, Energy Environ. Sci. 9 (2016) 155–163.

[29] M.T. Klug, A. Osherov, A.A. Haghighirad, S.D. Stranks, P.R. Brown, S. Bai, J.T.-W. Wang, X. Dang, V. Bulović, H.J. Snaith, A.M. Belcher, Tailoring metal halide perovskites through metal substitution: influence on photovoltaic and material properties, Energy Environ. Sci. 10 (2017) 236–246.

[30] X. Guo, C. McCleese, C. Kolodziej, A.C. Samia, Y. Zhao, C. Burda, Identification and characterization of the intermediate phase in hybrid organic inorganic $MAPbI_3$ perovskite, Dalton Trans. 45 (2016) 3806–3813.

[31] F. Hao, C.C. Stoumpos, Z. Liu, R.P. Chang, M.G. Kanatzidis, Controllable perovskite crystallization at a gas–solid interface for hole conductor-free solar cells with steady power conversion efficiency over 10%, J. Am. Chem. Soc. 136 (2014) 16411–16419.

[32] C.C. Stoumpos, C.D. Malliakas, M.G. Kanatzidis, Semiconducting tin and lead iodide perovskites with organic cations: phase transitions, high mobilities, and near-infrared photoluminescent properties, Inorg. Chem. 52 (2013) 9019–9038.

[33] T.J. Jacobsson, L.J. Schwan, M. Ottosson, A. Hagfeldt, T. Edvinsson, Determination of thermal expansion coefficients and locating the temperature-induced phase transition in methylammonium lead perovskites using X-ray diffraction, Inorg. Chem. 54 (2015) 10678–10685.

[34] A.K. Chilvery, A.K. Batra, B. Yang, K. Xiao, P. Guggilla, M. Aggarwal, R. Surabhi, R. Lal, J. Currie, B. Penn, Perovskites: transforming photovoltaics, a mini-review, J. Photonics Energy 5 (2015) 057402.

[35] H.J. Feng, T.R. Paudel, E.Y. Tsymbal, X.C. Zeng, Tunable optical properties and charge separation in $CH_3NH_3Sn_xPb_{1-x}I_3/TiO_2$-based planar perovskites cells, J. Am. Chem. Soc. 137 (2015) 8227–8236.

[36] T. Baikie, Y. Fang, J.M. Kadro, M. Schreyer, F. Wei, S.G. Mhaisalkar, M. Graetzel, T.J. White, Synthesis and crystal chemistry of the hybrid perovskite $(CH_3NH_3)PbI_3$ for solid-state sensitized solar cell applications, J. Mater. Chem. A 1 (2013) 5628–5641.

[37] P.S. Whitfield, N. Herron, W.E. Guise, K. Page, Y.Q. Cheng, I. Milas, M.K. Crawford, Structures, phase transitions and tricritical behavior of the hybrid perovskite methyl ammonium lead iodide, Sci. Rep. 6 (2016) 35685.

[38] M.N.F. Hoque, M. Yang, Z. Li, N. Islam, X. Pan, K. Zhu, Z. Fan, Polarization and dielectric study of methylammonium lead iodide thin film to reveal its nonferroelectric nature under solar cell operating conditions, ACS Energy Lett. 1 (2016) 142–149.

Ippili Swathi received her Integrated M.Sc. degree in Chemistry from Pondicherry University, India in 2013. She is currently pursuing her Ph.D. degree in Materials Science and Engineering Department in Chungnam National University, Republic of Korea under the supervision of Prof. Soon-Gil Yoon. Her research interests include the synthesis of perovskite materials, fabrication and development of energy harvesting devices.

Jella Venkatraju obtained his M.Sc. degree in department of Physics from Pondicherry University, India in 2012. Now he is a Ph.D. student under the supervision of Prof. Soon-Gil Yoon in the Department of Materials Science and Engineering from Chungnam National University, Republic of Korea. His interests of research include study of thermoelectric, piezoelectric materials and development of fusion energy harvesting device.

Jaegyu Kim received his MS degree in the department of Materials Science and Engineering at KAIST, S. Korea in 2016. Now he is a PhD candidate under the supervision of Prof. Hong in the department of Materials Science and Engineering at KAIST. His research interests are piezoelectric energy harvesting devices and domain imaging of ferroelectric materials

Prof. Seungbum Hong joined the Korea Advanced Institute of Science and Technology (KAIST), Korea, in 2017 as an associate professor in the Department of Materials Science and Engineering and created the Materials Imaging and Integration Laboratory. He received his BS degree in 1994, MS degree in 1996 and his PhD degree in 2000 in the field of nanoscale observation of ferroelectric thin films, both from KAIST. After completing postdoctoral research at the École Polytechnique Fédérale de Lausanne, Switzerland, from 2000 to 2001, he joined the probe storage project team as a project leader at the Samsung Advanced Institute of Technology in 2002. In 2007, he moved to Argonne National Laboratory as a staff scientist, and worked as a principal investigator in local domain and transport studies of oxide heterostructures and polymer ferroelectrics using atomic force microscopy until 2017.

Prof. Soon-Gil Yoon received his Ph.D. from the Korea Advanced Institute of Science and Technology (KAIST), Korea in 1988. He is a professor in Department of Materials Science and Engineering, Chungnam National University, Republic of Korea. His current research interests are Thin film capacitor, Fusion technology of Solar cell, Thermoelectric, and Piezoelectric using one material and one structure, In situ graphene growth with no transfer at 150 ^{o}C, Flexoelectric properties using Zn-Al:LDH nanosheets. Perovskite dye thin films such as $MAPbI_3$, $MASnI_3$, and $MAPbCl_3$, etc by CVD. He had published SCI papers of about 320 including Nano Letters, Advanced Materials, ACS Nano, Nano Energy, J. Mater. Chem. A, and Scientific Reports.